

1 **Resource limitation modulates the fate of dissimilated nitrogen in a dual-pathway**

2 **Actinobacterium**

3 David C. Vuono<sup>1,6</sup>, Robert W. Read<sup>1</sup>, James Hemp<sup>2</sup>, Benjamin W. Sullivan<sup>3</sup>, John A. Arnone  
4 III<sup>1</sup>, Iva Neveux<sup>1</sup>, Bob Blank<sup>4</sup>, Carl Staub<sup>5</sup>, Evan Loney<sup>1</sup>, David Miceli<sup>1</sup>, Mari Winkler<sup>6</sup>, Romy  
5 Chakraborty<sup>7</sup>, David A. Stahl<sup>6</sup>, Joseph J. Grzymiski<sup>1,\*</sup>

6 <sup>1</sup>Division of Earth and Ecosystem Sciences, Desert Research Institute, Reno, NV 89512, USA

7 <sup>2</sup>Division of Geological and Planetary Sciences, California Institute of Technology, Pasadena,  
8 CA, USA

9 <sup>3</sup>Department of Natural Resources and Environmental Science, University of Nevada, Reno, NV  
10 89557, USA

11 <sup>4</sup>Agricultural Research Service, U.S. Department of Agriculture, Reno, NV, 89512, USA

12 <sup>5</sup>Agtron, Inc. 9395 Double R Blvd, Reno, NV 89521, USA

13 <sup>6</sup>Department of Civil and Environmental Engineering, University of Washington, Seattle, WA,  
14 98195, USA

15 <sup>7</sup>Lawrence Berkeley National Laboratory, Berkeley, CA, 94729, USA

16 \*Correspondence: Joseph J. Grzymiski, Division of Earth and Ecosystem Sciences, Desert  
17 Research Institute, Reno, 2215 Raggio Parkway, NV 89512, USA

18 **Email: [Joe.Grzymiski@dri.edu](mailto:Joe.Grzymiski@dri.edu)**

## 19 **Abstract**

20 Respiratory ammonification and denitrification are two evolutionarily unrelated dissimilatory  
21 nitrogen (N) processes central to the global N cycle, the activity of which is thought to be  
22 controlled by carbon (C) to nitrate ( $\text{NO}_3^-$ ) ratio. Here we find that *Intrasporangium calvum* C5, a  
23 novel menaquinone-based dual-pathway denitrifier/respiratory ammonifier, disproportionately  
24 utilizes ammonification rather than denitrification when grown under carbon or nitrate limitation,  
25 not C: $\text{NO}_3^-$  ratio. Higher growth rates are promoted by ammonification and metabolite and  
26 transcriptional profiles during growth show that the bacterium produces its own formate from a  
27 fermentable carbon source (lactate) to further generate a proton motive force for the  
28 ammonification pathway. Transcript abundances encoding for nitrite reducing enzymes, NrfAH  
29 and NirK, also significantly increase in response to nitrite production. Mechanistically, our  
30 results suggest that pathway selection is driven by intracellular redox potential (redox poise),  
31 which may be lowered during resource limitation, thereby decreasing catalytic activity of  
32 upstream electron transport steps needed for denitrification enzymes. Our work advances our  
33 understanding of the biogeochemical flexibility of N-cycling organisms and pathway evolution.

## 34 **Introduction**

35 Globally, respiratory ammonification and denitrification are vital nitrogen (N) dissimilation  
36 pathways that either retain reactive N to support net primary productivity or close the N-cycle  
37 through the release of gaseous N, respectively [1]. The environmental controls on these two  
38 pathways, particularly the ratio of electron-donor to electron-acceptor (e.g., C: $\text{NO}_3^-$ ) [2], have  
39 gained attention [3–7] due to increased anthropogenic N inputs into the environment [8].  
40 However, the effects of resource limitation on growth and pathway selection (i.e., allocation of C  
41 and N to dissimilatory and assimilatory processes), which are often confounded by C: $\text{NO}_3^-$  ratio,  
42 have not been tested. Strong selective pressures from Earth's shifting biogeochemistry and  
43 oxidation-state have driven evolutionary adaptations to microbial electron transport chains (ETC)  
44 [9, 10], respiratory chain redox potentials [11–13], and protein atomic composition [14, 15], may  
45 shed light on how these pathways are regulated in contemporary organisms. Here, by identifying  
46 the biochemical and evolutionary differences between respiratory ammonification and

47 denitrification, we disentangle the functional significance and molecular mechanisms of electron  
48 transfer through either pathway in a dual pathway organism.

49 From a biochemical standpoint, the primary difference between respiratory ammonification and  
50 denitrification is their respective source of reducing equivalents in the ETC: 1) heme-based  
51 cytochrome c nitrite reductase used in respiratory ammonification receive electrons directly from  
52 the quinone (Q) pool [16] while 2) copper and *cd*<sub>1</sub> nitrite reductases used in denitrification  
53 receive electrons from a soluble electron carrier (e.g., cytochrome c) via the bc<sub>1</sub> complex [17].  
54 From an evolutionary standpoint, we can place each N-module's origin to a putative time in  
55 Earth history based on the metal co-factors that would have been bioavailable: heme-based  
56 cytochromes in an ancient, more reduced, environment compared to the copper-containing nitrite  
57 reductases in an oxidizing environment [18]. The bioenergetic chains of microorganisms also  
58 underwent selective pressure to shift from low-potential (LP) to high-potential (HP) quinones in  
59 response to Earth's oxygenation [11, 12]. Menaquinone (MK) is thought to be the ancestral type  
60 of LP quinone [19]. Organisms that use ubiquinone (UQ) are thought to have evolved under high  
61 O<sub>2</sub> tensions with  $\alpha$ -,  $\beta$ -,  $\gamma$ -proteobacteria as the only bacterial clades to use UQ [12]. Surprisingly,  
62 our understanding for the biochemistry of denitrification is based predominantly on HP UQ-  
63 based systems [20], leaving a significant knowledge gap in the physiology and biochemistry of  
64 LP MK-based denitrifiers and how they link electron transfer with energy capture under resource  
65 limitation [21–23].

66 In order to resolve the mechanisms of C:NO<sub>3</sub><sup>-</sup> control on pathway selection and better understand  
67 branched respiratory chains in LP-based nitrate-reducing organisms, we undertook the  
68 characterization of the novel Gram-positive Actinobacterium strain *Intrasporangium calvum* C5:  
69 a dual-pathway nitrite reducer that uses MK as sole pool quinone. Here we show that over a  
70 range of C:NO<sub>3</sub><sup>-</sup> ratios, duplicated at two substrate concentrations, *I. calvum* disproportionately  
71 utilizes its ammonia-forming pathway during C limitation ( $\leq 0.4$  mM lactate), when C:NO<sub>3</sub><sup>-</sup> ratios  
72 are  $< 1$  (an observation contrary to the current paradigm). Using a genome-guided approach  
73 coupled to time-series transcriptomics and metabolite profiles, we identified differentially  
74 expressed genes in the bacterium's ETC and central metabolic pathways. Using this information  
75 to inform a metabolic reconstruction of the ETC and extensive literature on the biochemistry of

76 the bc<sub>1</sub> complex, we propose a new mechanism by which these two pathways are regulated at the  
77 biochemical level.

## 78 **Materials and Methods**

### 79 **Culture Conditions**

80 Media preparation: All cultures were grown at 30 °C and shaken at 250 rpm. Nitrate reducing  
81 minimal media was prepared with the following final concentrations: NaCl (0.6mM), NH<sub>4</sub>Cl  
82 (1.75mM) (for ammonium replete conditions but not used in NH<sub>4</sub>-deplete conditions), MgCl<sub>2</sub>  
83 (0.2mM), CaCl<sub>2</sub> (0.04mM), KCl (0.1mM), K<sub>2</sub>HPO<sub>4</sub> (0.01mM), NaHCO<sub>3</sub>- (0.3mM), cysteine  
84 (1mM) as reducing agent, resazurin as redox indicator, and trace elements and trace vitamin  
85 solutions as reported [24, 25]. 1M sterile filtered (0.2µm) Concentrated stocks of 60% w/w  
86 sodium DL-lactate solution (Sigma-Aldrich, St. Louis, MO, USA), sodium-nitrate and sodium-  
87 nitrite (≥99%, Fisher Scientific, Pittsburg, PA, USA) were diluted into media prior to  
88 autoclaving to achieve the desired C:NO<sub>3</sub><sup>-</sup> ratio. C:NO<sub>3</sub><sup>-</sup> ratio was calculated based on [3] where  
89 the number of C atoms (n) in the e-donor is multiplied by the concentration of the e-donor,  
90 divided by the number of N atoms in the e-acceptor multiplied by the concentration of the e-  
91 acceptor (Table S4). See SI Materials and Methods for complete description of Hungate  
92 technique prepared media. Mean pH for all culture vessels (time series and end-point; Table S5),  
93 measured at the end of each experiment, was 7.3±0.05 (n=144).

### 94 **Analytical procedures**

95 Growth Curve/Cell counts/Yield Measurements: Growth curves were measured from scratch-  
96 free Balch-tubes grown cultures using an automated optical density reader at OD<sub>600</sub> nm  
97 (Lumenautix LLC, Reno, NV). End-point cultures were monitored until all replicates reached  
98 stationary phase (65-100 hours depending on C:NO<sub>3</sub><sup>-</sup> treatment) (Figure S6). Cell counts were  
99 performed by fixing cells in 4% paraformaldehyde (final concentration) for 20 minutes, filtered  
100 onto 0.2µm pore-sized black polycarbonate filters. A complete description is provided in SI  
101 Materials and Methods. Biomass concentrations were measured by filtration and drying as per  
102 standard protocol [26]. A complete description is provided in SI Materials and Methods.

103

104 Ion and Gas Chromatography Measurements: A dual channel Dionex ICS-5000+ (Thermo  
105 Scientific) ion chromatograph (IC) was used to measure organic (lactate, acetate, and formate)  
106 and inorganic (nitrite and nitrate) anions on an AS11-HC column and cations (ammonium) on a  
107 CS-16 column from the bacterial growth media. A complete description is provided in SI  
108 Materials and Methods.

### 109 **Phylogenetic, Genomic, and Transcriptomic Analysis**

110 Genomic DNA was assembled using Canu (version 1.7.1) with an estimated genome size of 5  
111 million base pairs [27]. The resulting single contiguous fragment was aligned to the *I. calvum*  
112 7KIP genome (Acc: NC\_014830.1) to compare sequence similarity in Mauve[28, 29]. Genome  
113 annotation for C5 was performed through the NCBI Prokaryotic Genome pipeline  
114 ([www.ncbi.nlm.nih.gov/genome/annotation\\_prok/](http://www.ncbi.nlm.nih.gov/genome/annotation_prok/)). Additional gene prediction analysis and  
115 functional annotation was performed by the DOE Joint Genome Institute (JGI) using the Isolate  
116 Genome Gene Calling method (Prodigal V2.6.3 February, 2016) under the submission ID  
117 172966. The complete genome sequence and annotation is available in the NCBI database under  
118 the BioProject number PRJNA475609. A complete description of the phylogenetic, pathway  
119 analysis, and cost-minimization calculations is provided in SI Material and Methods. For  
120 transcriptomic analysis, the resulting raw reads were inspected using FastQC [30] to determine  
121 quality, read length, and ambiguous read percentage. Reads were trimmed based on quality score  
122 with a sliding window of 5 base pairs, quality cutoff of 28, trailing cutoff quality score of 10, as  
123 well as adapter contamination removal in Trimmomatic [31]. A complete description is provided  
124 in SI Materials and Methods. Statistical analyses were conducted in the R environment for  
125 statistical computing (r-project.org). Data that was tested using parametric statistical analysis  
126 were first validated for normality by visualizing the data as a histogram and testing via Shapiro-  
127 Wilks test for normality.

### 128 **Results**

129 **Genomic analysis of *I. calvum* C5.** We sequenced and analyzed the genome of *I. calvum* C5 to  
130 first compare its similarity to the type species *I. calvum* 7KIP. We identified a high degree of  
131 sequence similarity to 7KIP based on three homologous sequence regions as locally collinear  
132 blocks (SI Results). Genome size of C5 was 4,025,044 base pairs (bp), only 662 bp longer than

133 7KIP. Genomic analysis of the ETC revealed the typical suite of complexes common to  
134 facultative aerobes, including primary dehydrogenases (*nuo* complex, succinate dehydrogenase),  
135 alternative *NDH-2* NADH dehydrogenase, cytochrome  $bc_1$  complex, high-oxygen adapted  
136 cytochrome c oxidase (A-family), and low-oxygen adapted cytochrome *bd* oxidase. The  $bc_1$   
137 complex subunits are also located immediately upstream of cytochrome c oxidase, suggesting  
138 that these enzymes are encoded in a single operon creating a supercomplex. Despite *I. calvum*'s  
139 seeming propensity for aerobic growth on a number of growth media [32], its bioenergetic  
140 system uses MK as its sole pool quinone. *I. calvum* also possesses multiple pathways for  
141 supplying electrons into the MK-pool, such as formate, malate, hydroxybutyrate, and  
142 glycerophosphate dehydrogenases. Once in the MK-pool, there are alternative pathways for  
143  $MKH_2$  oxidation that can circumvent the  $bc_1$  complex, such as a membrane-bound respiratory  
144 nitrate reductase module (NarG). In addition, to NarG, its dissimilatory N module composition  
145 consists of a truncated denitrification pathway ( $N_2O$  is a terminal product) using a copper nitrite  
146 reductase NirK and quinol-dependent nitric oxide reductase qNor. *I. calvum* also possesses both  
147 catalytic and membrane anchor subunits (NrfA and NrfH, respectively) for a pentaheme  
148 cytochrome c module involved in respiratory nitrite ammonification.

149 ***I. calvum* encodes for a functional NrfAH complex and assimilates  $NH_4^+$  via respiratory**  
150 **nitrite ammonification.** To gain insight into possible function of the NrfAH complex, we  
151 aligned the NrfA protein sequences from C5 and 7KIP to a collection of 33 recognized  
152 cytochrome c nitrite reductases from published annotated genomes (Table S1). This confirmed  
153 that NrfA from *I. calvum* is a member of the CxxCH 1<sup>st</sup> heme motif group (Figure 1A), which  
154 forms one of four clades on the NrfA phylogenetic tree. We then queried the genomes of the taxa  
155 in our phylogeny for other annotated N-reducing modules used in nitrate reduction, nitrite  
156 reduction, NO-forming nitrite reduction, and primary pool quinone. Among the three major  
157 clades of NrfA, at least 5 additional taxa are noted having dissimilatory N-module inventories  
158 containing dual respiratory pathways: *S. thermophilum*, *B. azotoformans*, *B. bataviensis*, *B.*  
159 *bacteriovorus*, and *Candidatus N. inopinata*, (Figure 1A). None of the taxa in our NrfA  
160 phylogeny harbored the *cd*<sub>1</sub> nitrite reductases (NirS). Due to the exclusive NirK representation in  
161 dual-pathway membership, we asked whether there might be differences in protein atomic  
162 composition between NirK and NrfA, given the disparate evolutionary origins of these modules  
163 [33]. We collected 20 additional publicly available NirK protein sequences from nondual-

164 pathway denitrifiers (Table S1) and calculated the protein C and N composition for our  
165 NirK/NrfA collection as atoms per residue side-chain (Figure 1B). These results showed a  
166 significant depletion in C and N per residue side-chain for NirK compared to NrfA (C and N:  
167  $p < 0.001$ ; t-test), indicating that resource constraints are imprinted on the evolution of these  
168 proteins.

169 We next tested the functionality of *I. calvum*'s Nrf complex by growing the bacterium under  
170 reducing conditions (8 mM lactate, 12 mM nitrate, ammonium-replete). We then performed a  
171 state-transition where biomass from late-exponential growth phase was collected and  
172 anaerobically inoculated into ammonia-deplete media (Figure 1C; SI Results). Despite no  
173 detectable amounts of ammonium produced in the media over time, cell counts increased  
174  $5.4 \times 10^5 \pm 8.9 \times 10^4$  cells/mL (0.126  $\pm$  0.02 optical absorbance at OD<sub>600</sub>) over a 48-hour incubation,  
175 indicating consumption of ammonium produced by NrfA. Net ammonium production was  
176  $13 \pm 2.7$   $\mu$ moles with the remainder of dissimilated N being used by the denitrification pathway  
177 ( $24 \pm 4.2$   $\mu$ moles N<sub>2</sub>O-N), resulting in a recovery of 97.4% dissimilated N. These results  
178 confirmed that *I. calvum* C5 has a functional Nrf complex and also consumes the product  
179 (ammonium) of respiratory nitrite ammonification.

180 **Respiratory nitrite ammonification exceeds denitrification under C-limitation.** We  
181 investigated C:NO<sub>3</sub><sup>-</sup> control on respiratory ammonification versus denitrification on cultures of *I.*  
182 *calvum* C5 over a high resource C:NO<sub>3</sub><sup>-</sup> range (16-0.4 mM lactate, 12 mM nitrate; ratio 4-0.1)  
183 and low resource C:NO<sub>3</sub><sup>-</sup> range (1.6-0.04 mM lactate, 1.2 mM nitrate; ratio 4-0.1). This  
184 experimental design enabled us to evaluate C:NO<sub>3</sub><sup>-</sup> control over a broader range than previous  
185 studies that only considered ratios  $\geq 1.5$  [3, 4, 34], while also testing the effects of resource  
186 concentration on pathway selection. Under all the treatments tested, gas and ion chromatography  
187 measurements showed products of both respiratory pathways, differing only in the relative  
188 fraction of N<sub>2</sub>O versus ammonium production across treatments (Figure 2). At high resource  
189 concentrations, respiratory ammonification did not prevail at high C:NO<sub>3</sub><sup>-</sup> ratios (Figure 2A,  
190 Figure 2B, left panels; Table S2). Instead, significantly greater amounts of N<sub>2</sub>O were produced  
191 over ammonium, though nitrite was still the major extracellular end-product of nitrate  
192 respiration. Despite the predominance of N<sub>2</sub>O production under the high resource concentrations,

193 ammonium production exceeded N<sub>2</sub>O production only at the lowest C:NO<sub>3</sub><sup>-</sup> ratio (0.4 mM  
194 lactate, ratio=0.1) (Figure 2) and accounted for 76.2±0.1% of dissimilated N.

195 Results from the low resource dataset provided weak support for the strict stoichiometry  
196 hypothesis that C:NO<sub>3</sub><sup>-</sup> controls pathway selection. Ammonia exceeded N<sub>2</sub>O production only  
197 under one high C:NO<sub>3</sub><sup>-</sup> ratio treatment (ratio=4; 1.6 mM lactate; Figure 2A, Figure 2B, right  
198 panels). However, at ratios ≤1 (≤0.4 mM lactate), significantly more ammonium than N<sub>2</sub>O was  
199 produced. On average, respiratory ammonification accounted for 78.1±8.9% of dissimilated N  
200 for lactate concentrations ≤0.4 mM. When these results are taken in context with cell physiology,  
201 we observed a significant and positive relationship between specific growth rate ( $\mu$ ) and the  
202 fraction of N dissimilated by respiratory ammonification ( $R^2=0.5$ ;  $p<0.001$ ) (Figure 2C, S1;  
203 Table S3).

204 **Resource concentration influences the metabolite profiles of ammonium and N<sub>2</sub>O**  
205 **production.** Given the co-occurrence of end products from both pathways during the end-point  
206 experiments (Figure 2), we next investigated the timing of ammonium and N<sub>2</sub>O production  
207 relative to metabolite profiles for lactate, nitrate/nitrite, and growth phase at two resource  
208 concentrations with the same ratio (8 mM and 0.8 mM lactate, ratio=2; Figure 1A, Figure S2,  
209 Figure S3). Despite ample e-donor and e-acceptor available for growth, the high resource  
210 cultures entered a quasi-stationary phase at ~50 hours, after which there was continued slow  
211 growth (Figure 1A). Metabolite profiles showed that ammonium and N<sub>2</sub>O production began  
212 simultaneously, as soon as nitrite was produced from nitrate reduction. The low resource cultures  
213 entered stationary phase at ~40 hours (Figure S2) after nitrate had been fully utilized. No further  
214 cell growth was observed after stationary phase was reached. These results show that cell growth  
215 occurred primarily on the reduction of nitrate, while nitrite reduction to ammonium and N<sub>2</sub>O  
216 occurred during a stationary growth phase, demonstrating that microbial activity is not always  
217 correlated with growth. The metabolite profiles for ammonium and N<sub>2</sub>O at low resources (Figure  
218 S2) did not mirror those observed at high resources (Figure 2A). The rate of N<sub>2</sub>O production  
219 significantly decreased and ammonium production oscillated rather than steadily increase  
220 through time. These differences in metabolite profiles, further demonstrate that concentration  
221 influences the activities of pathway bifurcation. Repeated time series experiments that were  
222 extended up to 300 hours show that nitrite is slowly depleted, but does not get fully consumed



223 (Figure S3). When cultures were given nitrite, instead of nitrate as a terminal electron acceptor (8  
224 mM lactate, 12 mM nitrite; ratio=2), we observed no immediate growth (as was observed with  
225 nitrate) but measured more N<sub>2</sub>O than ammonium production (33.4±4.8 μmoles N<sub>2</sub>O-N and  
226 8.0±2.5 μmoles NH<sub>4</sub><sup>+</sup>, respectively) (Figure S4), demonstrating respiratory ammonification does  
227 not exceed denitrification when nitrite is supplied as the sole acceptor in *I. calvum*.

228 **Nitrite-reducing modules are up-regulated during late exponential- and stationary-phase**  
229 **growth.** In order to gain insight into mechanisms of gene regulation and transcriptional  
230 organization of *I. calvum*, we conducted RNA-Seq in parallel with the high resource time-series  
231 metabolite profile (Figure 3A). This approach enabled us to compare genome-wide differential  
232 expression based on log<sub>2</sub> fold change (lfc) of RNA extracted from three growth phases: early  
233 exponential (EE), late exponential (LE), and stationary (ST) (Figure 3B, Figure S5). Within the  
234 central metabolic pathway beginning with the conversion of lactate to pyruvate, we observed a  
235 moderate decrease in transcript abundance of L-lactate dehydrogenase (LDH) (Intca\_16740)  
236 between EE-LE and -ST (lfc = -1.6±0.7; -1.9±0.7), respectively. Lactate utilization protein C  
237 (LUP) (Intca\_04080), an enzyme involved in lactate degradation, also showed a moderate and  
238 significant decrease in transcript abundance between EE-LE and -ST (lfc = -1.6±0.6; -2.4±0.6,  
239 *p*=0.002), respectively. *I. calvum* encodes for two parallel metabolic pathways for pyruvate  
240 conversion to acetyl-CoA: pyruvate dehydrogenase (PDH) (Intca\_01255) and pyruvate  
241 ferredoxin oxidoreductase (PFOR) (Intca\_15510). For PDH, there was a significant and  
242 moderate increase in transcript abundance between EE-LE and -ST (lfc = 2.1±0.6, *p*=0.002;  
243 1.5±0.6), respectively. For PFOR, there was a minor decrease in transcript abundance between  
244 EE-LE (lfc = -0.43±0.5), and then a moderate increase in transcript abundance between EE-ST  
245 (1.1±0.5). Citrate synthase (Intca\_04135), the enzyme catalyzing the conversion of acetyl-CoA  
246 to citrate and the first step of the tricarboxylic acid (TCA) cycle, showed a highly significant  
247 increase in transcript abundance between EE-LE and -ST (lfc = 4.3±0.5, *p*<0.001; 6.9±0.5,  
248 *p*<0.001).

249 Within the ETC, there was moderate and significant decrease in transcript abundance for all  
250 subunits from the primary dehydrogenase (*nuo* complex; Intca\_03465-03539) between EE-LE  
251 and -ST (lfc = -1.2±0.3; -2.4±0.6, *p*<0.001), respectively. Nitrate reductase subunits showed no  
252 change in transcript abundance between EE-LE (lfc = 0.01±0.07) and moderately decreased in

253 abundance by ST (lfc =  $-1.2 \pm 0.1$ ), which was corroborated by the depletion of nitrate during  
254 stationary phase. There was a significant increase in transcript abundance of *nirK* (Intca\_17170)  
255 (lfc =  $2.2 \pm 0.6$ ,  $p=0.003$ ;  $2.4 \pm 0.6$ ,  $p<0.001$ ) and quinol dehydrogenase/membrane anchor subunit  
256 *nrfH* (Intca\_09465) (lfc =  $2.5 \pm 0.6$ ,  $p=0.001$ ;  $2.1 \pm 0.6$ ,  $p=0.003$ ) by EE-LT and EE-ST,  
257 respectively, which coincided with nitrite production (Figure 3A). The catalytic subunit of the  
258 cytochrome c nitrite reductase complex (*nrfA*) (Intca\_09460) also increased moderately in  
259 transcript abundance by EE-LT and EE-ST (lfc =  $1.6 \pm 0.6$ ;  $1.0 \pm 0.6$ ), respectively (Figure 3B).  
260 Contrary to the transcript abundance patterns of *nirK* and *nrfAH*, nitric oxide reductase (qNor;  
261 Intca\_01525) transcripts moderately increased between EE-LT (lfc =  $1.6 \pm 0.6$ ) but decreased in  
262 the successive time periods (lfc =  $0.43 \pm 0.6$  between EE-ST; lfc =  $-1.2 \pm 0.6$  between LE-ST)  
263 (Figure 3B).

264 There was a significant increase in transcript abundance of formate transporter *focA*  
265 (Intca\_17150) between EE-ST, as well as LE-ST (lfc =  $4.9 \pm 0.7$ ,  $p=0.002$ ;  $4.8 \pm 0.7$ ,  $p=0.002$ ;  
266 respectively). We verified the production of formate in our ion chromatography measurements in  
267 the range of 100-200 $\mu$ M following late exponential growth. We also observed a moderate  
268 increase in transcript abundance of formate dehydrogenase (FDH) subunits (Intca\_11150-  
269 11160). These results implicate the activity of formate oxidation, which would contribute to a  $\Delta p$   
270 in the periplasm via a Q-loop mechanism and the reduction of MK for electron transfer to nitrite  
271 via cytochrome c nitrite reductase. Considering that formate was not provided in our media  
272 recipe, an alternative pathway for formate production must exist in *I. calvum*. We also observed  
273 acetate production in similar concentrations as formate (100-200 $\mu$ M). In *E. coli*, formate is  
274 produced anaerobically from the action of pyruvate formate lyase (PFL). We identified a putative  
275 PFL based on genome annotation (Intca\_12230), where transcript abundance also significantly  
276 increased by ST. PFL is also highly sensitive to oxygen [35], which was also in agreement with a  
277 significant increase in transcript abundance between EE-ST and LE-ST (Figure 3B) of  
278 cytochrome *bd* oxidase (Intca\_01110 and Intca\_01115), which is thought to protect anaerobic  
279 enzymes against oxidative stress [36].

## 280 Discussion

281 We challenge the paradigm that C:NO<sub>3</sub><sup>-</sup> ratio controls pathway selection in a dual-pathway  
282 organism based on a simple principle: ratios do not account for the abundance of growth-limiting

283 resources. We hypothesized that limitation in C or  $\text{NO}_3^-$  should better predict pathway selection  
284 in a dual-pathway denitrifier/respiratory ammonifier. To test this hypothesis, we systematically  
285 measured the response of the Gram-positive Actinobacterium *Intrasporangium calvum* C5 to the  
286 same range of C: $\text{NO}_3^-$  ratios at both high and low resource loadings to better resolve mechanisms  
287 of pathway selection. We demonstrated that resource concentration, not C: $\text{NO}_3^-$  ratio, influences  
288 pathway selection. We found stronger support for respiratory ammonification preference under  
289 C-limitation (at low C: $\text{NO}_3^-$  ratios), which also grew at significantly higher growth rates (Figure  
290 2). These results suggest that the NrfA complex, which receives electrons directly from the MK-  
291 pool, is optimized to maximize power when one or more resources are limiting. These data,  
292 together with metabolic reconstructions from metabolite and transcriptional profiles (Figure 3),  
293 suggest that C: $\text{NO}_3^-$  ratio alone is insufficient to explain pathway selection.

294 The theoretical basis for pathway selection is explained by the law of the minimum (LM) and the  
295 maximum power principle (MPP), which state that growth is limited by the least abundant  
296 resource and that biological systems are designed to maximize power in order to effectively  
297 allocate energy to reproduction and survival [37, 38], respectively. Here, it appears these two  
298 natural theories are working together: when resources are limited, the cell utilizes the respiratory  
299 pathway for growth that is optimized to maximize power. Power, in this case, is realized as  
300 higher growth rates from the cultures exhibiting disproportionately higher ammonium production  
301 than  $\text{N}_2\text{O}$  production (Figure 2: high resources: C: $\text{NO}_3^-$  ratio = 0.1; low resources: C: $\text{NO}_3^-$  ratios  
302 = 4, 1, 0.5, 0.1). More specifically, the bacterium must generate a greater  $\Delta p$  in order to  
303 maximize power when starved for a growth limiting resource. This may help to further explain  
304 how respiratory ammonification, which is overall energetically less favorable than denitrification  
305 (lactate with nitrite:  $\Delta G^\circ = -763.98$  versus  $\Delta G^\circ = -1196.93$ , respectively), can have higher growth  
306 yields [39] and growth rates (Figure 2, Figure S1) under C- and N-limitation due to the higher  
307 energy yield on a per-nitrite basis (denitrification: -217 KJ per mole nitrite; respiratory  
308 ammonification: -399 KJ per mole nitrite). For comparison, a total of 8  $\text{H}^+$  are translocated  
309 during denitrification by *I. calvum* (not including nitrate reduction since both pathways share this  
310 step) (Figure 3): NADH dehydrogenase translocates 4  $\text{H}^+$  per  $\text{MKH}_2$  oxidized and the  $\text{bc}_1$   
311 complex translocates an additional 4  $\text{H}^+$  per  $\text{MKH}_2$  oxidized. However, 2  $\text{H}^+$  must be consumed  
312 in the periplasm to reduce nitrite to  $\text{NO}$  [40]. qNor has a net zero  $\text{H}^+$  release (consumes 2  $\text{H}^+$  to  
313 make  $\text{N}_2\text{O}$  but releases 2  $\text{H}^+$ ) without  $\text{MKH}_2$  regeneration [41]. Thus, a net total of 6  $\text{H}^+$  are

314 translocated per nitrite reduced in denitrification with added biosynthetic costs of making the bc<sub>1</sub>  
315 complex and qNor. In respiratory ammonification, MK/MKH<sub>2</sub> redox pair is cycled between  
316 NADH dehydrogenase and formate dehydrogenase. 6 electrons and 8 H<sup>+</sup> are needed to reduce  
317 nitrite to ammonium, thus 3 MKH<sub>2</sub> are needed [16]. If MKH<sub>2</sub> is received from NADH  
318 dehydrogenase, 12 H<sup>+</sup> are translocated plus 2 H<sup>+</sup> from FDH. As each MKH<sub>2</sub> is oxidized at the  
319 binding site of NrfH, 2 H<sup>+</sup> are liberated [16], resulting in a net total of 12 H<sup>+</sup> translocated per  
320 nitrite reduced for respiratory ammonification. This implies that the cell might deplete its NADH  
321 pool more rapidly on a per nitrite basis. However, if more protons are pumped in the early stages  
322 of growth, the cell would be allocating the ATP generated for anabolism, as evidenced by higher  
323 growth rates in the cultures exhibiting higher amounts of respiratory ammonification (Figure 2),  
324 which is supported by the MPP.

325 Under our high resource conditions (Figure 2; left panels), at C:NO<sub>3</sub><sup>-</sup> ratios ≥ 1, we observed that  
326 denitrification prevailed and these cultures had lower growth rates than the predominantly  
327 ammonium producing cultures. These high resource circumstances resulted in the production of  
328 toxic intermediates (i.e., NO<sub>2</sub><sup>-</sup> and possibly NO, albeit at undetectable levels), which may explain  
329 why these cultures had lower growth rates (Figure 2; left panels) and quasi-steady state growth  
330 curves in our high resource metabolite profile (Figure 3A). Rowley and colleagues [42] reported  
331 that at least 20% of the N<sub>2</sub>O released during high C conditions were produced by competition  
332 between nitrite and nitrate in the active-site of NarG. Under excess C concentrations, NarG  
333 produces intracellular NO from NO<sub>2</sub><sup>-</sup> and these intermediates are likely inhibitory to cell growth,  
334 which may explain why our growth curves (Figure 3A) reached a quasi-steady state before  
335 nitrate had been fully utilized (as compared to the low resource metabolite profile, Figure S2).  
336 Furthermore, resources were not limiting growth under these conditions. Rather, the cells were  
337 likely experiencing toxicity from NO and NO<sub>2</sub><sup>-</sup> and thus the metabolic outcomes would be  
338 beyond the scope of the LM and MPP. Nonetheless, these results clearly demonstrate that end-  
339 product formation from the two resource concentrations tested, with the same C:NO<sub>3</sub><sup>-</sup> ratios, are  
340 not identical thereby refuting the C:NO<sub>3</sub><sup>-</sup> control hypothesis.

341 We selected a single treatment (8 mM lactate, 12 mM nitrate; C:NO<sub>3</sub><sup>-</sup> ratio = 2), in which we  
342 observed both denitrification and respiratory ammonification occurring simultaneously, for  
343 RNA-Seq in order to gain insight into the transcriptional organization of actively growing *I.*

344 *calvum* cells (Figure 3). Strangely, we saw a decrease in transcript abundance encoding for two  
345 enzymes known to convert lactate to pyruvate, LDH and LUP. While normalized read counts  
346 (Figure S5) were generally consistent across growth phases, indicative of constitutive expression,  
347 further research investigating the mode of anaerobic lactate oxidation in *I. calvum* would  
348 illuminate how reducing equivalents are fed into its central metabolic pathway. For example, *S.*  
349 *loihica* PV-4 is known to use lactate for both denitrification and respiratory ammonification, but  
350 only uses acetate for denitrification [24]. Nonetheless, our transcriptomic data suggests that  
351 pyruvate plays a central role in providing reducing equivalents to the TCA cycle as Acetyl-CoA,  
352 as evidenced by significant upregulation in the genes encoding for pyruvate dehydrogenase and  
353 citrate synthase, as well as apparent “leaking” via incomplete lactate oxidation through the  
354 release of acetate and formate. Such leaking may be produced by a putative PFL, adding to the  
355 diversity of C utilization pathways feeding the ETC, and thereby driving pathway selection for  
356 nitrite reduction. Our transcriptomic results, coupled with a parallel metabolite profile (Figure 3),  
357 also suggest that the dual-pathway is induced by the presence of nitrite, and is not constitutively  
358 expressed like nitrate reductase, *narG*. Furthermore, it appears that the significant increase in  
359 transcript abundance for the gene encoding the *bd* oxidase helps to protect the anaerobic-  
360 dependent biochemical machinery against oxidative stress, thereby scavenging any residual  
361 oxygen during anaerobic growth.

362 Our metabolite profiles for N oxyanion respiration and N<sub>2</sub>O versus ammonium production show  
363 conflicting patterns relative to previous studies (Figure 3A, Figure S2). Yoon and colleagues [43]  
364 reported complete reduction of nitrate, production of nitrite, and then rapid consumption of  
365 nitrite, with N<sub>2</sub>O as the main end-product, by *S. loihica* PV-4 (5 mM lactate, 1 mM nitrate;  
366 ratio=0.6). When Yoon and colleagues [43] replaced nitrate with nitrite as the dominant electron  
367 acceptor (5 mM lactate, 1 mM nitrite, ratio=0.6), ammonification prevailed. Other research has  
368 shown the same response to nitrite replacement and ammonification dominance using non-  
369 fermentable C-sources (i.e., acetate) in chemostat enrichments of *Geobacter lovleyi*[44]. In our  
370 work, nitrite was never fully depleted (Figure 3A, Figure S2, Figure S3) and when nitrite was  
371 given as the only electron acceptor, the bacterium predominantly used denitrification but without  
372 concurrent growth (Figure S4). Similar to our work, Kraft and colleagues[34] also reported  
373 denitrification dominance when nitrite was supplied as the terminal acceptor. These differences

374 highlight an incomplete understanding for the molecular mechanisms underlying the framework  
375 put forth by the LM and MPP.

376 A detailed look into the biochemistry of ETC complexes helps to shed light on the molecular  
377 mechanisms modulating pathway bifurcation. For example, Yoon and colleagues [3]  
378 demonstrated that elevated pH selects for ammonification in *S. loihica* PV-4. This phenotypic  
379 response is due to a decrease in the midpoint potential of the Rieske protein at higher pH [45–  
380 48]. Thus, any hindrance of electron flow through the bc<sub>1</sub> complex would ultimately reduce the  
381 activity of downstream processes and promote alternative respiratory pathways. Nitrogen and C  
382 limitation have also been shown to influence flux distributions in redox sensitive proteins,  
383 including those found in electron transport [49]. A drop in the intracellular redox potential (redox  
384 poise) of the cell due to resource limitation may decrease the midpoint potential of the Rieske  
385 protein and reduce the activity of any downstream electron exit modules, such as NirK [50–52].  
386 Thus, based on fundamental principles of protein redox chemistry and thermodynamics, it  
387 becomes clear that denitrification versus ammonification are likely not modulated by an arbitrary  
388 ratio of C:NO<sub>3</sub><sup>-</sup>, but rather by thermodynamic constraints of the Q-cycle [11, 12]. The phenotypic  
389 response of higher rates of denitrification over ammonification at high C:NO<sub>3</sub><sup>-</sup> ratios in other  
390 published studies [3, 4] may also be due to enrichment bias for organisms that utilize quinones  
391 with higher midpoint potentials in their bioenergetic chains (Figure 1). Bergdoll and colleagues  
392 [11] suggested that comparisons of Rieske/cytb complexes from organisms with high- and low-  
393 potential quinones may help to reconcile the thermodynamic properties of Q-cycle function.  
394 However, most of our understanding of denitrification bioenergetics is based on evolutionarily  
395 recent UQ-based HP bioenergetic chains from Gram-negative  $\alpha$ -,  $\beta$ -,  $\gamma$ -proteobacteria. Because *I.*  
396 *calvum* uses a MK-based LP bioenergetic chain it may be possible that the differences in  
397 pathway selection across treatments are unique to LP chains.

398 Piecing together the evolutionary history of the N-cycle using isotopic signatures for  
399 geochemically available N module cofactors (i.e., Ni, Fe, and Mo) coupled to molecular  
400 evolutionary analysis has revealed respiratory ammonification was likely a major component of  
401 the Archean N-cycle [33]. Abiotic nitrite formation and depletion of ammonia through  
402 photodissociation [53] would have created selective pressures for a dissimilatory N pathway that  
403 also produced assimilatory N. We demonstrate that NrfA proteins are significantly enriched in N

404 compared to NirK (i.e., no evolutionary constraints to cost minimize N in the *nrfA* gene product  
405 [15]) (Figure 1B) and that ammonium production (without accumulation in the medium)  
406 supports growth in *I. calvum* (Figure 1C). The Nrf module is also relatively simplistic in that it  
407 receives electrons directly from the quinol pool and not the bc<sub>1</sub> complex used in denitrification.  
408 The early exit of electrons from the ETC (i.e., before reaching the bc<sub>1</sub> complex) suggests that Nrf  
409 may have originated prior to the bc<sub>1</sub> complex. Furthermore, the quinol oxidation site (Q<sub>o</sub>) of  
410 cytochrome *b* contains a PDWY motif, indicative of an ancestral LP respiratory chain found in  
411 many Gram-positive organisms [54]. However, there is still debate regarding the presence of a  
412 cytochrome *bc* complex in the last universal common ancestor [54, 55]. Lastly, the Nrf module is  
413 wired to operate via a q-loop with formate dehydrogenase whose Mo-cofactors would have also  
414 been bioavailable during the Archean, further supporting an early evolution.

415 In summary, we employ a new predictive framework that accounts for the biochemistry and  
416 evolutionary history of N modules, ETC complexes, and pool quinones to suggest the  
417 mechanisms by which these two pathways are regulated at the molecular level. With this  
418 understanding, it may be possible to extend our framework to environmental microbial  
419 populations and accelerate model development across different ecosystem scales (i.e., cross-scale  
420 systems biology).

421 **ACKNOWLEDGMENTS.** We thank F. von Netzer, K. Hunt, S Morales, N. Stopnisek, K. Meinhardt, W. Qin, N  
422 Elliot, T. Hazen, H. Carlson, B. Ramsey, A. Murray, Z. Harrold, T. Morgan, and P. Longley for thoughtful feedback  
423 and discussions. This research was supported by a grant from the Nevada Governor's Office of Economic  
424 Development (JG), by the Desert Research Institute (DRI) postdoctoral research fellowship program, and in part by  
425 Ecosystems and Networks Integrated with Genes and Molecular Assemblies (ENIGMA) (<http://enigma.lbl.gov>)—a  
426 Scientific Focus Area Program at Lawrence Berkeley National Laboratory under contract number DE-AC02-  
427 05CH11231 and funded in part by Oak Ridge National Laboratory under contract DE-AC05-00OR22725, and is  
428 based upon work supported by the U.S. Department of Energy, Office of Science, Office of Biological &  
429 Environmental Research.

### 430 **Competing Interests**

431 The authors declare no conflicts of interest

### 432 **References**

433 1. Knowles R. Denitrification. *Microbiol Rev* 1982; **46**: 43–70.

- 434 2. Tiedje JM, Sextstone AJ, Myrold DD, Robinson JA. Denitrification: ecological niches , competition and  
435 survival. *Antonie Van Leeuwenhoek* 1982; **48**: 569–583.
- 436 3. Yoon S, Cruz-García C, Sanford R, Ritalahti KM, Löffler FE. Denitrification versus respiratory  
437 ammonification: Environmental controls of two competing dissimilatory NO<sub>3</sub><sup>-</sup>/NO<sub>2</sub><sup>-</sup> reduction pathways in  
438 *Shewanella loihica* strain PV-4. *ISME J* 2015; **9**: 1093–1104.
- 439 4. van den Berg EM, van Dongen U, Abbas B, van Loosdrecht MC. Enrichment of DNRA bacteria in a  
440 continuous culture. *ISME J* 2015; **9**: 2153–2161.
- 441 5. Schmidt CS, Richardson DJ, Baggs EM. Constraining the conditions conducive to dissimilatory nitrate  
442 reduction to ammonium in temperate arable soils. *Soil Biol Biochem* 2011; **43**: 1607–1611.
- 443 6. Hardison AK, Algar CK, Giblin AE, Rich JJ. Influence of organic carbon and nitrate loading on partitioning  
444 between dissimilatory nitrate reduction to ammonium (DNRA) and N<sub>2</sub> production. *Geochim Cosmochim*  
445 *Acta* 2015; **164**: 146–160.
- 446 7. Fazzolari É, Nicolardot B, Germon JC. Simultaneous effects of increasing levels of glucose and oxygen  
447 partial pressures on denitrification and dissimilatory nitrate reduction to ammonium in repacked soil cores.  
448 *Eur J Soil Biol* 1998; **34**: 47–52.
- 449 8. Galloway JN, Aber JD, Erisman JW, Seitzinger SP, Howarth RW, Cowling EB, et al. The Nitrogen  
450 Cascade. *Bioscience* 2003; **53**: 341.
- 451 9. Moparthy VK, Hägerhäll C. The evolution of respiratory chain complex i from a smaller last common  
452 ancestor consisting of 11 protein subunits. *J Mol Evol* 2011; **72**: 484–497.
- 453 10. Dibrova D V., Cherepanov DA, Galperin MY, Skulachev VP, Mulkidjanian AY. Evolution of cytochrome  
454 bc complexes: From membrane-anchored dehydrogenases of ancient bacteria to triggers of apoptosis in  
455 vertebrates. *Biochim Biophys Acta - Bioenerg* 2013; **1827**: 1407–1427.
- 456 11. Bergdoll L, Ten Brink F, Nitschke W, Picot D, Baymann F. From low- to high-potential bioenergetic chains:  
457 Thermodynamic constraints of Q-cycle function. *Biochim Biophys Acta* 2016; **1857**: 1569–1579.
- 458 12. Schoepp-Cothenet B, Lieutaud C, Baymann F, Verméglio A, Friedrich T, Kramer DM, et al. Menaquinone  
459 as pool quinone in a purple bacterium. *Proc Natl Acad Sci* 2009; **106**: 8549–54.
- 460 13. Soo RM, Hemp J, Parks DH, Fischer WW, Hugenholtz P. On the origins of oxygenic photosynthesis and  
461 aerobic respiration in Cyanobacteria. *Science (80- )* 2017; **355**: 1436–1440.
- 462 14. Baudouin-Cornu P, Schuerer K, Marlière P, Thomas D. Intimate evolution of proteins: Proteome atomic  
463 content correlates with genome base composition. *J Biol Chem* 2004; **279**: 5421–5428.
- 464 15. Grzymalski JJ, Dussaq AM. The significance of nitrogen cost minimization in proteomes of marine  
465 microorganisms. *ISME J* 2012; **6**: 71–80.
- 466 16. Einsle O, Messerschmidt A, Huber R, Kroneck PMH, Neese F. Mechanism of the six-electron reduction of  
467 nitrite to ammonia by cytochrome c nitrite reductase. *J Am Chem Soc* 2002; **124**: 11737–11745.
- 468 17. Kraft B, Strous M, Tegetmeyer HE. Microbial nitrate respiration - Genes, enzymes and environmental  
469 distribution. *J Biotechnol* 2011; **155**: 104–117.
- 470 18. Godfrey L V., Falkowski PG. The cycling and redox state of nitrogen in the Archaean ocean. *Nat Geosci*  
471 2009; **2**: 725–729.
- 472 19. Nitschke W, Dracheva S. Reaction center associated cytochromes in Anoxygenic Photosynthetic Bacteria.  
473 In: Blankenship R, Madigan M, Bauer C (eds).1995. Kluwer Academic, Dordrecht, The Netherlands, pp  
474 775–805.



- 475 20. Lalucat J, Bennasar A, Bosch R, Garcia-Valdes E, Palleroni NJ. Biology of *Pseudomonas stutzeri*.  
476 *Microbiol Mol Biol Rev* 2006; **70**: 510–547.
- 477 21. Suharti, de Vries S. Membrane-bound denitrification in the Gram-positive bacterium *Bacillus azotoformans*.  
478 *Biochem Soc Trans* 2005; **33**: 130–133.
- 479 22. Heylen K, Keltjens J, Stein LY. Redundancy and modularity in membrane-associated dissimilatory nitrate  
480 reduction in *Bacillus*. *Front Microbiol* 2012; **3**: 1–27.
- 481 23. Decleyre H, Heylen K, Bjorn T, Willems A. Highly diverse nirK genes comprise two major clades that  
482 harbour ammonium-producing denitrifiers. *BMC Genomics* 2016; **17**: 1–13.
- 483 24. Yoon S, Sanford RA, Löffler FE. *Shewanella* spp. Use acetate as an electron donor for denitrification but  
484 not ferric iron or fumarate reduction. *Appl Environ Microbiol* 2013; **79**: 2818–2822.
- 485 25. Hillesland KL, Lim S, Flowers JJ, Turkarslan S, Pinel N, Zane GM, et al. Erosion of functional  
486 independence early in the evolution of a microbial mutualism. *Proc Natl Acad Sci* 2014; **111**: 14822–14827.
- 487 26. APHA. Standard Methods for the Examination of Water and Wastewater, 23rd ed. 2012. American Public  
488 Health Association: Washington, DC.
- 489 27. Koren S, Walenz BP, Berlin K, Miller JR, Bergman NH, Phillippy AM. Canu : scalable and accurate long-  
490 - read assembly via adaptive k - - mer weighting and repeat separation. *Genome Res* 2017; 1–35.
- 491 28. Darling ACE, Mau B, Blattner FR, Perna NT. Mauve : Multiple Alignment of Conserved Genomic  
492 Sequence With Rearrangements. *Genome Res* 2004; **14**: 1394–1403.
- 493 29. Darling AE, Mau B, Perna NT. Progressivemaue: Multiple genome alignment with gene gain, loss and  
494 rearrangement. *PLoS One* 2010; **5**: e11147.
- 495 30. Andrews S. FastQC: A quality control tool for high throughput sequence data. Available online at: [http://](http://www.bioinformatics.babraham.ac.uk/projects/fastqc)  
496 [www.bioinformatics.babraham.ac.uk/projects/fastqc](http://www.bioinformatics.babraham.ac.uk/projects/fastqc) 2010.
- 497 31. Bolger AM, Lohse M, Usadel B. Trimmomatic: A flexible trimmer for Illumina sequence data.  
498 *Bioinformatics* 2014; **30**: 2114–2120.
- 499 32. Kalakoutskii LV, Kirillova IP, Krassilnikov NA. a New Genus of the. *J Gen Microbiol* 1967; **48**: 373-79–  
500 85.
- 501 33. Klotz MG, Stein LY. Nitrifier genomics and evolution of the nitrogen cycle. *FEMS Microbiol Lett* 2008;  
502 **278**: 146–156.
- 503 34. Kraft B, Tegetmeyer HE, Sharma R, Klotz MG, Ferdelman TG, Hettich RL, et al. The environmental  
504 controls that govern the end product of bacterial nitrate respiration. *Science (80- )* 2014; **345**: 676–679.
- 505 35. Abbe KS, Takahashi S, Yamada T. Involvement of oxygen-sensitive pyruvate-formate lyase in mixed-acid  
506 fermentation by *Streptococcus mutans* under strictly anaerobic conditions. *J Bacteriol* 1982; **152**: 175.
- 507 36. Das A, Silaghi-Dumitrescu R, Ljungdahl LG, Kurtz DM. Cytochrome *bd* oxidase, oxidative stress, and  
508 dioxygen tolerance of the strictly anaerobic bacterium *Moorella thermoacetica*. *J Bacteriol* 2005; **187**:  
509 2020–2029.
- 510 37. Lotka AJ. Contribution to the Energetics of Evolution. *Proc Natl Acad Sci* 1922; **8**: 147–151.
- 511 38. DeLong JP. The maximum power principle predicts the outcomes of two-species competition experiments.  
512 *Oikos* 2008; **117**: 1329–1336.
- 513 39. Strohm TO, Griffin B, Zumft WG, Schink B. Growth yields in bacterial denitrification and nitrate

- 514 ammonification. *Appl Environ Microbiol* 2007; **73**: 1420–1424.
- 515 40. Zumft WG. Cell biology and molecular basis of denitrification. *Microbiol Mol Biol Rev* 1997; **61**: 533–616.
- 516 41. Hemp J, Gennis RB. Diversity of the Heme-Copper Superfamily in Archaea: Insights from Genomics and  
517 Structural Modeling. In: Schäfer G, Penefsky HS (eds). *Results and Problems in Cell Differentiation*. 2008.  
518 Springer Science+Business Media, pp 1–28.
- 519 42. Rowley G, Hensen D, Felgate H, Arkenberg A, Appia-ayme C, Prior K, et al. Resolving the contributions of  
520 the membrane-bound and periplasmic nitrate reductase systems to nitric oxide and nitrous oxide production  
521 in *Salmonella enterica* serovar Typhimurium. *Biochem J* 2012; **762**: 755–762.
- 522 43. Yoon S, Sanford RA, Löffler FE. Nitrite control over dissimilatory nitrate/nitrite reduction pathways in  
523 *Shewanella loihica* strain PV-4. *Appl Environ Microbiol* 2015; **81**: 3510–3517.
- 524 44. van den Berg EM, Rombouts JL, Kuenen JG, Kleerebezem R, van Loosdrecht MCM. Role of nitrite in the  
525 competition between denitrification and DNRA in a chemostat enrichment culture. *AMB Express* 2017; **7**:  
526 1–7.
- 527 45. Link TA, Hagen WR, Pierik AJ, Assmann C, von Jagow G. Determination of the redox properties of the  
528 Rieske cluster of bovine heart bc1 complex by direct electrochemistry of a water- soluble fragment.  
529 *EurJBiochem* 1992; **208**: 685–691.
- 530 46. Ugulava NB, Crofts AR. CD-monitored redox titration of the Rieske Fe-S protein of *Rhodobacter*  
531 *sphaeroides*: pH dependence of the midpoint potential in isolated bc1 complex and in membranes. *FEBS Lett*  
532 1998; **440**: 409–413.
- 533 47. Zu Y, Couture MMJ, Kolling DRJ, Crofts AR, Eltis LD, Fee JA, et al. Reduction Potentials of Rieske  
534 Clusters: Importance of the Coupling between Oxidation State and Histidine Protonation State. *Biochemistry*  
535 2003; **42**: 12400–12408.
- 536 48. Trumpower BL. Cytochrome bc1 complexes of microorganisms. *Microbiol Rev* 1990; **54**: 101–129.
- 537 49. Ansong C, Sadler NC, Hill EA, Lewis MP, Zink EM, Smith RD, et al. Protein redox dynamics during light-  
538 to-dark transitions in cyanobacteria and impacts due to nutrient limitation. *Front Microbiol* 2014; **5**: 1–10.
- 539 50. Snyder CH, Merbitz-Zahradnik T, Link TA, Trumpower BL. Role of the Rieske Iron – Sulfur Protein  
540 Midpoint Potential in the Protonmotive Q-Cycle Mechanism of the Cytochrome bc 1 Complex. *J Bioenerg*  
541 *Biomembr* 1999; **31**: 235–242.
- 542 51. Denke E, Merbitz-Zahradnik T, Hatzfeld OM, Snyder CH, Link TA, Trumpower BL. Alteration of the  
543 midpoint potential and catalytic activity of the Rieske iron-sulfur protein by changes of amino acids forming  
544 hydrogen bonds to the iron-sulfur cluster. *J Biol Chem* 1998; **273**: 9085–9093.
- 545 52. Hunte C, Solmaz S, Palsdóttir H, Wenz T. A structural perspective on mechanism and function of the  
546 cytochrome bc1 complex. In: Schäfer G, Penefsky HS (eds). *Results and Problems in Cell Differentiation*.  
547 2008. Springer Science+Business Media, pp 253–270.
- 548 53. Falkowski PG. Evolution of the nitrogen cycle and its influence on the biological sequestration of CO<sub>2</sub> in  
549 the ocean. *Nature* 1997; **387**: 272–275.
- 550 54. Kao WC, Hunte C. The molecular evolution of the Qo Motif. *Genome Biol Evol* 2014; **6**: 1894–1910.
- 551 55. Dibrova D V., Cherepanov DA, Galperin MY, Skulachev VP, Mulkidjanian AY. Evolution of cytochrome  
552 bc complexes: From membrane-anchored dehydrogenases of ancient bacteria to triggers of apoptosis in  
553 vertebrates. *Biochim Biophys Acta - Bioenerg* 2013; **1827**: 1407–1427.
- 554 56. White D. The physiology and biochemistry of prokaryotes, 3rd ed. 2000. Oxford University Press.

- 555 57. Thauer RK, Jungermann K, Decker K. Energy conservation in chemotrophic anaerobic bacteria. *Bacteriol*  
556 *Rev* 1977; **41**: 100–180.
- 557 58. Giardina CP, Ryan MG. Total belowground carbon allocation in a fast-growing Eucalyptus plantation  
558 estimated using a carbon balance approach. *Ecosystems* 2002; **5**: 487–499.
- 559 59. Edgar RC. MUSCLE: multiple sequence alignment with high accuracy and high throughput. *Nucleic Acids*  
560 *Res* 2004; **32**: 1792–7.
- 561 60. Tamura K, Peterson D, Peterson N, Stecher G, Nei M, Kumar S. MEGA5: Molecular evolutionary genetics  
562 analysis using maximum likelihood, evolutionary distance, and maximum parsimony methods. *Mol Biol*  
563 *Evol* 2011; **28**: 2731–2739.
- 564 61. Stamatakis A. RAxML version 8: A tool for phylogenetic analysis and post-analysis of large phylogenies.  
565 *Bioinformatics* 2014; **30**: 1312–1313.
- 566 62. Kelley LA, Mezulis S, Yates C, Wass M, Sternberg M. The Phyre2 web portal for protein modelling,  
567 prediction, and analysis. *Nat Protoc* 2015; **10**: 845–858.
- 568 63. Dobin A, Davis CA, Schlesinger F, Drenkow J, Zaleski C, Jha S, et al. STAR: Ultrafast universal RNA-seq  
569 aligner. *Bioinformatics* 2013; **29**: 15–21.
- 570 64. Liao Y, Smyth GK, Shi W. FeatureCounts: An efficient general purpose program for assigning sequence  
571 reads to genomic features. *Bioinformatics* 2014; **30**: 923–930.
- 572 65. Love MI, Huber W, Anders S. Moderated estimation of fold change and dispersion for RNA-seq data with  
573 DESeq2. *Genome Biol* 2014; **15**: 1–21.
- 574

## 575 **Figure legends**

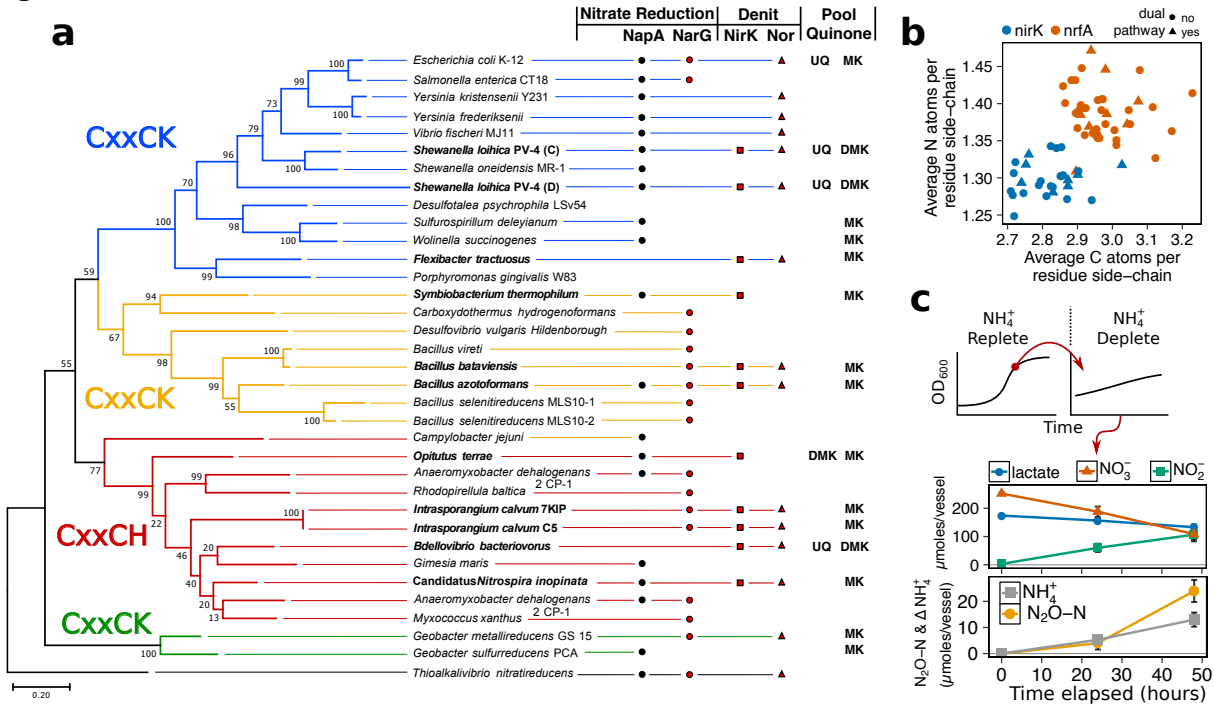
576 **Figure 1.** (A) Maximum likelihood phylogenetic tree of NrfA amino acid sequences from known  
577 respiratory ammonifiers and accompanying N-module composition for each organism. Pool  
578 quinone is also noted for dual-pathway nitrite reducers and model species. Colors of the main  
579 branches denote the 1<sup>st</sup> heme motif type: CxxCK and CxxCH. (B) Protein atomic composition  
580 for N and C normalized to protein length for NirK and NrfA nitrite reductases. (C) State-  
581 transition from ammonium-replete to ammonium-deplete for *I. calvum* C5 grown under 8mM  
582 lactate 12mM nitrate minimal media at 30 °C. Metabolite profiles for ammonium-deplete are  
583 shown.

584  
585 **Figure 2.** The effects of high resource (left; range of lactate concentrations with 12 mM NO<sub>3</sub><sup>-</sup>)  
586 and low resource (right; range of lactate concentrations with 1.2 mM NO<sub>3</sub><sup>-</sup>) concentrations with  
587 the same C:NO<sub>3</sub><sup>-</sup> ratio on pathway selection in *I. calvum* C5. (A) Production of N<sub>2</sub>O-N and net  
588 change of NH<sub>4</sub><sup>+</sup> over a 100-hour incubation period at 30 °C. Each bar represents the average of  
589 8-10 replicates per treatment (Table S5). (B) Fraction of dissimilated N by pathway. (C) Growth  
590 rates for each corresponding treatment. The x-axis label defines lactate concentration and C:NO<sub>3</sub><sup>-</sup>  
591 ratio in parentheses.

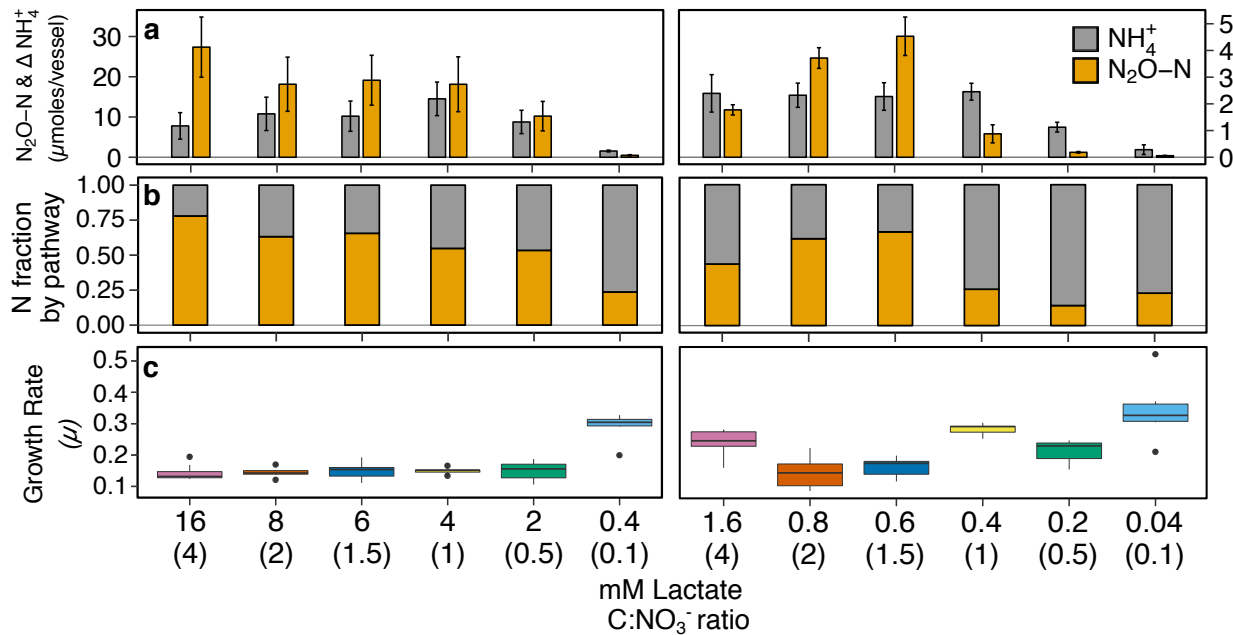
592  
593 **Figure 3.** (A) Time-series metabolite profiles for lactate, nitrate, and nitrite (top pane),  
594 production of dissimilated end-products as N<sub>2</sub>O-N and net change in NH<sub>4</sub><sup>+</sup> ammonium  
595 production (middle pane), and corresponding growth curve of *I. calvum* cells grown under 8mM  
596 lactate 12mM nitrate (C:NO<sub>3</sub><sup>-</sup> ratio = 2) (bottom pane). Sampling points during growth phases  
597 are marked for transcriptomic analysis. (B) Metabolic reconstruction of the ETC from *I. calvum*  
598 with transcriptional changes for genes participating in dual-pathway dissimilatory nitrite  
599 reduction. Log<sub>2</sub> fold changes in transcript abundance are shown for late exponential relative to  
600 early exponential growth phase (EE vs. LE), stationary phase relative to early exponential  
601 growth phase (EE vs. ST), and stationary phase relative to late exponential growth phase (LE vs.  
602 ST). Locus IDs for each gene product correspond to heat map subplots in the order shown (left-  
603 to-right for each growth phase and top-to-bottom for each locus ID specified). Higher transcript  
604 abundance is represented in red, lower transcript abundance in blue, and no change in transcript  
605 abundance in white. Significant changes in transcript abundance ( $p < 0.01$ ) are marked as a red  
606 box. Value of log<sub>2</sub> fold change is specified within each subplot. The log<sub>2</sub> fold changes of 14  
607 NADH dehydrogenase subunits (Intca\_03465-03530) were averaged as transcriptional changes  
608 were all shifted in the same direction.

609

610 **Figures**



611  
612 **Figure 1.**  
613



614  
615 **Figure 2.**

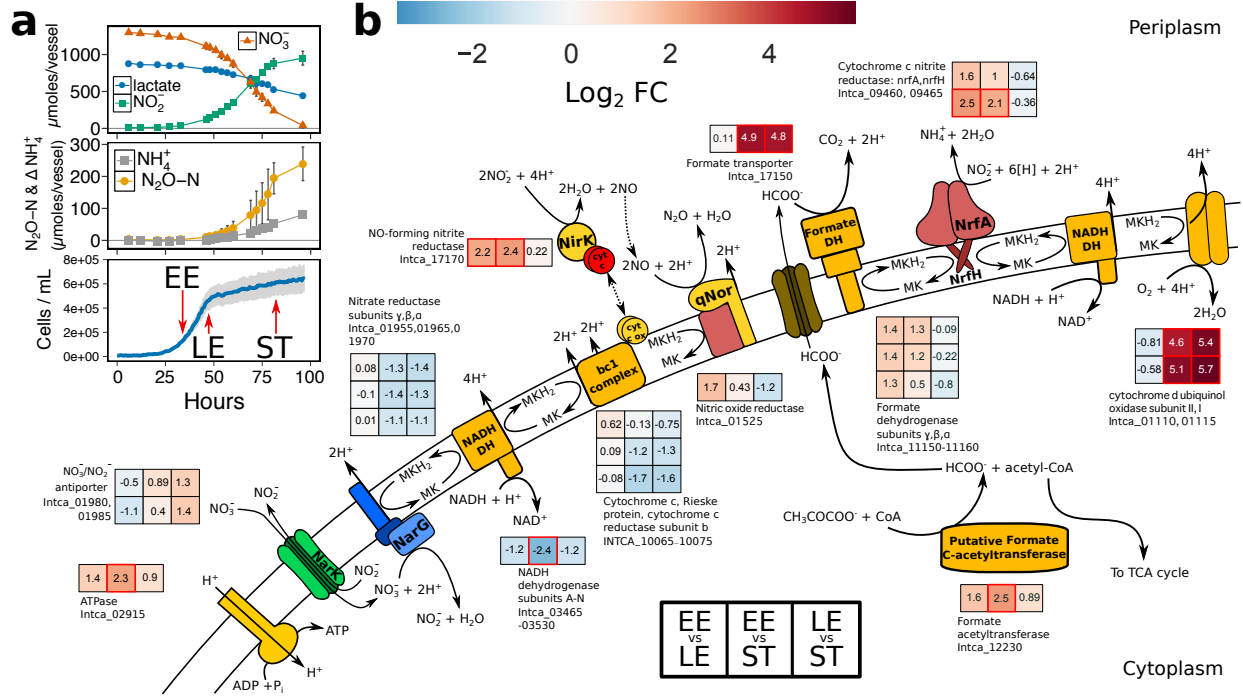


Figure 3.